Crimping-induced structural gradients explain the lasting strength of poly L-lactide bioresorbable vascular scaffolds during hydrolysis

Karthik Ramachandran[a], Tiziana Di Luccio[a,b], Artemis Ailianou[a], Mary Beth Kossuth[c], James P. Oberhauser[c,1], and Julia A. Kornfield[a,2]

[a]Division of Chemistry and Chemical Engineering, California Institute of Technology, Pasadena, CA 91125; [b]Division of Sustainable Materials, ENEA Centro Ricerche Portici, I-80055 Portici, Italy; and [c]Global Product Development, Abbott Vascular, Santa Clara, CA 95054

Edited by Frank S. Bates, University of Minnesota, Minneapolis, MN, and approved August 17, 2018 (received for review May 9, 2018)

Biodegradable polymers open the way to treatment of heart disease using transient implants (bioresorbable vascular scaffolds, BVSs) that overcome the most serious complication associated with permanent metal stents—late stent thrombosis. Here, we address the long-standing paradox that the clinically approved BVS maintains its radial strength even after 9 mo of hydrolysis, which induces a ∼40% decrease in the poly L-lactide molecular weight (*Mn*). X-ray microdiffraction evidence of nonuniform hydrolysis in the scaffold reveals that regions subjected to tensile stress during crimping develop a microstructure that provides strength and resists hydrolysis. These beneficial morphological changes occur where they are needed most—where stress is localized when a radial load is placed on the scaffold. We hypothesize that the observed decrease in *Mn* reflects the majority of the material, which is undeformed during crimping. Thus, the global measures of degradation may be decoupled from the localized, degradation-resistant regions that confer the ability to support the artery for the first several months after implantation.

PLLA | hydrolysis | coronary heart disease | BVS | X-ray microdiffraction

Coronary heart disease (CHD) restricts the flow of blood to the heart muscles due to the accumulation of plaque on the walls of the arteries surrounding the heart. Cardiovascular disease (CVD) accounted for 31% of all deaths worldwide in 2010 (1) and claimed more lives than all cancers combined in the United States in 2015 (2)—with over 40% of all CVD deaths due to CHD (1). The current standard of care for CHD is to implant a drug-eluting metal stent (DES) to hold the vessel open [>1 million implanted in 2008 in the United States alone (3)]. However, the rigid nature of metal stents permanently restricts arterial vasomotion and induces potentially fatal complications such as late stent thrombosis (LST) (4, 5). Bioresorbable vascular scaffolds (BVSs, Fig. 1*A*) are emerging as an alternative that, unlike metal stents, temporarily support the occluded artery for 6–9 mo and are completely resorbed in 2–3 y (6–8). Five-year follow-up in the first-in-man trials for BVS (101 patients, 2009) reported restoration of arterial vasomotion and dilation with no incidence of LST in properly deployed and well-apposed scaffolds (9–11). However, the second randomized clinical trial for BVS (335 patients, 2011–2013) indicated an increase in thrombosis (within 1 y) for BVS compared with DES (12), motivating further improvements. The greater thickness of BVS (∼150 μm) relative to metal stents (∼80 μm) may contribute to the reported increase in thrombosis (13). The key to thinner scaffolds is increased strength that lasts at least 3 mo after implantation, motivating the present study of the relationships between scaffold microstructure, mechanical strength, and hydrolytic degradation during the first 18 mo after deployment.

The structural material of the first clinically approved BVS [CE Mark in 2011 (4), FDA approval in 2016 (14)] is the semicrystalline polymer poly L-lactide (PLLA), which hydrolyzes into L-lactic acid and is metabolized by the body (15–18). Pure PLLA is a surprising choice for a BVS as it is widely described as a brittle material (literature values of fracture strain <10% at physiological conditions) (19, 20). PLLA blends (21, 22) and copolymers (23–25) that offer superior ductility failed to progress to the clinic as they prematurely lose strength due to relatively rapid hydrolysis (26, 27). The usual brittle character of PLLA was overcome via careful selection of processing conditions to impart ductile character to a BVS that remains strong for the first 9 mo after implantation. Manufacture of a BVS begins with a nearly amorphous PLLA preform (a tube with an inner diameter, ID, of 0.64 mm and outer diameter, OD, of 1.69 mm) (28) that is transformed into a vascular scaffold by a sequence of "tube expansion" (biaxial elongation into a uniform, thin-walled, oriented, glassy tube with an OD of 3.5 mm and thickness of ∼150 μm), "laser-cutting" a strut lattice from the tube, and "crimping" onto a balloon catheter (28, 29). Recent microdiffraction measurements reveal that this processing history creates important structural transformations during crimping (we return to this in *Discussion*) that facilitate deployment without fracture (28). However, surviving deployment is only the first step for a BVS toward clinical success; it is imperative for the deployed scaffold to maintain radial strength in the artery for an additional 3–6 mo despite hydrolytic degradation.

In agreement with the literature on PLLA (30), molecular weight (*Mn*) reduction of BVSs in vitro matches that in vivo (*SI*

Significance

The molecular basis of the mysterious ability of the clinically approved bioresorbable vascular scaffold to maintain radial strength after 9 mo of hydrolysis—despite a ∼40% reduction in the poly L-lactide molecular weight *Mn*—is an unexpected gradient in degradation revealed by X-ray microdiffraction. Hydrolysis is slowest in the 100- × 30-μm region where stress is concentrated during arterial contractions. This favorable gradient in hydrolysis arises from gradients in morphology created during crimping onto the angioplasty balloon: Small regions that undergo elongational deformation (<3% of scaffold) resist hydrolysis after deployment. This remarkably small amount of material (too low to detect in *Mn* measurements) has a disproportionate impact on strength because it forms precisely where the scaffold is most vulnerable to failure.

Author contributions: K.R. and J.A.K. designed research; K.R. and T.D.L. performed research; A.A., M.B.K., and J.P.O. contributed new reagents/analytic tools; K.R. and J.A.K. analyzed data; and K.R. and J.A.K. wrote the paper.

Conflict of interest statement: M.B.K. and J.P.O. are employees of Abbott Vascular. Funding for this research was provided by Abbott Vascular.

This article is a PNAS Direct Submission.

Published under the PNAS license.

[1]Present address: Gilead Sciences, Inc., Foster City, CA 94404.

[2]To whom correspondence should be addressed. Email: jakornfield@cheme.caltech.edu.

This article contains supporting information online at www.pnas.org/lookup/suppl/doi:10.1073/pnas.1807347115/-/DCSupplemental.

Published online September 17, 2018.

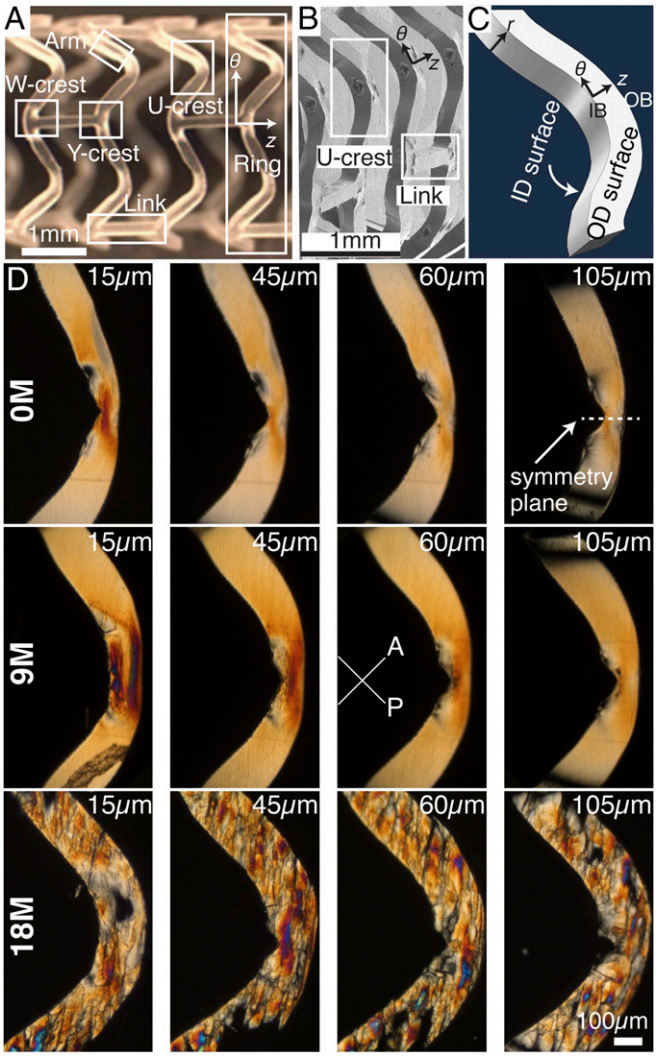

Fig. 1. Microscopy provides a coarse-grain map of the impact of hydrolysis on the microstructure of BVSs. (*A*) An optical micrograph of a deployed BVS defining the terms "W-crest," "Y-crest," "link," "arm," "U-crest," and "ring." Adapted from ref. 6, with permission from Elsevier. (*B*) Scanning electron micrograph highlighting diamond-shaped voids in U-crests after deployment. (*C*) Schematic diagram of a U-crest indicating the IB, where the voids occur, the OB, and the OD surface; the ID surface is hidden. (*D*) Polarized light micrographs (orientation of analyzer and polarizer shown as A and P) reveal structural anisotropies in 15-μm-thick sections cut from scaffolds hydrolyzed for 0 mo (0 M), 9 mo (9 M) and 18 mo (18 M). The distance shown indicates the position of each section relative to the ID (e.g., the 0 M–15 μm section is 15 μm from the ID). The retardation of the as-deployed scaffold (0 M) is highest in the region between the diamond-shaped void and the OB and increases with radial position from the OD to ID (retardation ∼400 nm near the OD and ∼500 nm at the ID); this gradient in retardation is still present after 9 M hydrolysis (*D*, 9 M) and has its origins in scaffold manufacture (see origin of *r*-gradient in retardation in *SI Appendix*). In contrast, the retardation does not systematically vary from the OD to ID after 18 M of hydrolysis.

Appendix, Fig. S1*A*), suggesting that the strength and structure observed during hydrolysis in vitro are relevant to hydrolysis in vivo as well. For the material and processing conditions examined here, deployed BVSs maintain their radial strength for more than 9 mo (*SI Appendix*, Fig. S1 *D* and *E*) (31); this is surprising in view of the substantial decrease of *Mn* over this time period (*SI Appendix*, Fig. S1 *A* and *B*), which is associated with scission of "tie chains" that connect lamellar crystals and provide load-bearing capability to the polymer (19, 32). The apparent disconnect between the strength and *Mn* of PLLA during hydrolysis is well documented (26, 33–35), but to the best of our knowledge there is no study that reconciles this discrepancy. The intriguing combination of *Mn* decrease without loss of strength is even more puzzling in light of a recent study that found extensive degradation and loss of strength in less than 4 mo of hydrolysis in scaffolds made from a different grade of PLLA and under different processing conditions (36). Here, we use X-ray microdiffraction to shed light on microstructural features that play a critical role in mitigating the effects of hydrolysis and provide lasting strength to the clinically approved BVS.

Results

We focus on the effects of hydrolysis at U-crests (defined in Fig. 1 *A* and *B*) as these regions are the most susceptible to fracture under loading. We compare the structure of scaffolds that have been crimped, deployed, and hydrolyzed for 9 mo (9 M) and 18 mo (18 M) to the as-deployed scaffold (0 M) to understand the progression of hydrolysis in the BVS. We describe hydrolysis effects starting with the more extreme 18 M case, which captures the PLLA microstructure as the scaffold begins to disintegrate, and then the more nuanced 9 M case, where the microstructure is still strong enough to support the artery. We begin by examining polarized light micrographs of ∼15-μm-thick sections of U-crests cut from the ID to the OD of the scaffolds (ID/OD indicated in Fig. 1*C*). Specifically, the micrographs reveal three types of regions based on the deformation imposed on them during crimping: The vast majority of the material is undeformed (e.g., arms, defined in Fig. 1*A*), a small region near the inner bend (IB, defined in Fig. 1*C*) is compressed along the θ direction, and a small region near the outer bend (OB, defined in Fig. 1*C*) is elongated in the θ direction. Within this context, we move to synchrotron X-ray microdiffraction results, which reveal gradients in the progression of hydrolysis that are distinct for each of the three types of regions.

Polarized light micrographs of 18 M sections reveal a material that is brittle, heterogeneous (e.g., 18 M, Fig. 1*D*; the bright blue-green microdomains have retardation >600 nm), and riddled with fissures preferentially oriented along the θ direction [18 M, Fig. 1*D*; see *SI Appendix*, Fig. S2 for micrographs cut from other (n = 3) 18 M scaffolds]. In contrast, the 9 M sections maintain structural integrity and, apart from a subtle increase in retardation, appear similar to their 0 M counterparts (Fig. 1*D*). In the vicinity of the diamond-shaped void of the U-crest (Fig. 1*B*), the 9 M sections have regions that appear orange-red (high retardation), indicating a material of stronger-than-average orientation. Regions that appear pale gray to black on the IB on either side of the diamond-shaped void indicate a material with low orientation in the plane of the section that is present upon deployment (0 M) and remains after 9 M hydrolysis. These strong variations in structure are consistently observed in 0 M and 9 M scaffolds (n = 3 for each; *SI Appendix*, Figs. S3 and S4) and are confined to a region that extends ∼100 μm to each side of the symmetry plane (defined in 0 M, Fig. 1*D*, *Right*). Therefore, we take advantage of the fine spatial resolution of X-ray microdiffraction (200-nm spot size) to probe the microstructure in these localized regions to find clues to the lasting strength of the BVS.

Consistent with the literature (26, 27, 37), 18 M of hydrolysis produces a decrease in amorphous content and a concomitant increase in crystallinity: The intensity of the amorphous halo at 18 M is approximately half that of 0 M (compare 18 M with 0 M in Figs. 2 and 3 and *SI Appendix*, Fig. S5*B*, *Left*) and the intensity of the (110)/(200) peaks increases dramatically (approximately threefold increase at 18 M relative to 0 M, Figs. 2 and 3 and *SI Appendix*, Fig. S5*C*, *Left*). Microdiffraction data acquired on the bright blue-green microdomains (18 M, Fig. 1*D*) indicate that these regions possess a greater number of oriented crystalline unit cells compared with the surrounding material (*SI Appendix*, Fig. S7). In contrast, a scaffold made with a different grade of PLLA, manufacturing process, and strut geometry undergoes rapid degradation and shows loss of

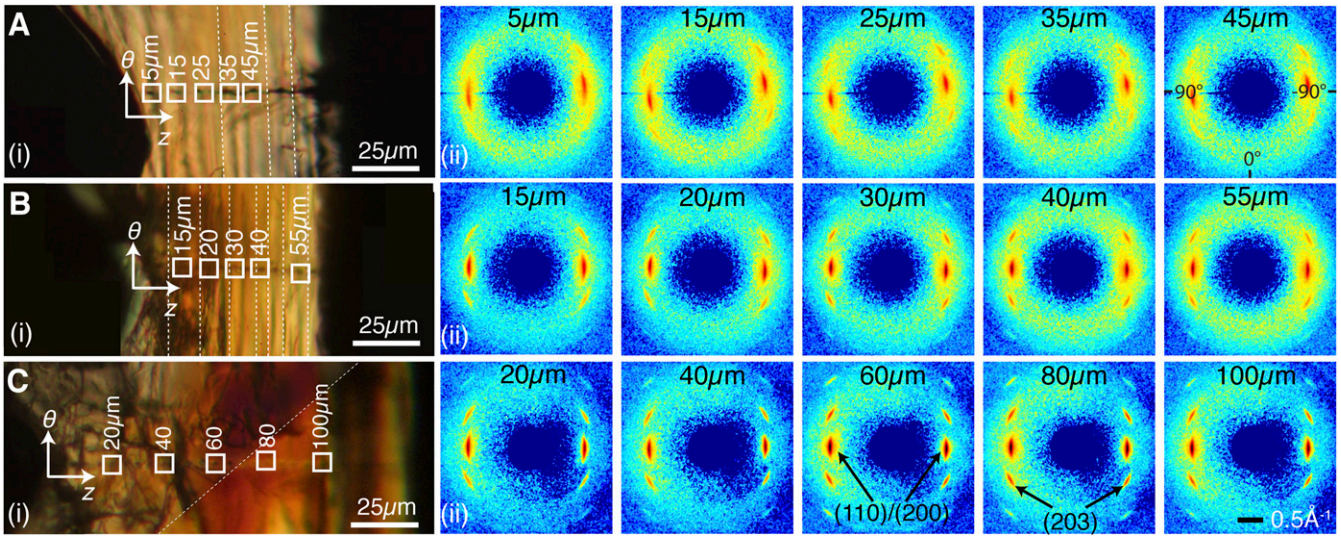

Fig. 2. Selected wide-angle X-ray microdiffraction patterns for the 15-μm-thick section cut at a radial position ∼60 μm from the ID for BVSs subjected to hydrolysis for (*A*) 0 M, (*B*) 9 M, and (*C*) 18 M. (*i*) Polarized light micrographs show the position of microdiffraction acquisitions (white squares labeled with their distance from the IB correspond to patterns in *ii*; white dashed lines indicate where images focused on specific X-ray marks were stitched together). (*ii*) Two-dimensional diffraction patterns use an identical logarithmic color scale [colors vary from 0 (deep blue) to 3 (deep red) counts] and *q*-scale (indicated at bottom right). Corresponding 1D patterns are given in Fig. 3 and quantitative characteristics of the amorphous and crystalline features of the 2D patterns are presented in *SI Appendix*, Fig. S5. Due to the structural discontinuities that develop after 18 mo of hydrolysis, the path from the IB to the OB of the 18 M section is nearly twice that of its 0 M or 9 M counterpart (∼120 μm from IB to OB in *C*, *i* compared with ∼60 μm in *A* and *B*, *i*).

crystallinity and orientation in the interior within 110 d of hydrolysis (36). Microdiffraction data on the clinically approved scaffold at 18 M (540 d) indicate an increase in the degree of crystallinity and retention of strong orientation along the θ direction (*SI Appendix*, Fig. S5 *C* and *D*, *Left* and *SI Appendix*, Figs. S8 and S9).

The differences that result from 9 mo of hydrolysis are less obvious, particularly for diffraction patterns acquired near the OB (compare 0 M and 9 M patterns, Fig. 2, *Right*). At 0 M, scattering patterns acquired at the symmetry plane are nearly indistinguishable for all microdiffraction positions (see *SI Appendix*, Figs. S10 and S11 for X-ray data and *SI Appendix*, Fig. S12 for quantitative characteristics of all five 0 M sections). However, at the 9 M symmetry plane, there is a clear gradient in morphology from the IB to the OB: The amorphous halo at the IB is ∼20% lower relative to the OB, which has intensity comparable to that of the as-deployed scaffold (compare 0 M with 9 M, Figs. 2 and 3 for microdiffraction data and *SI Appendix*, Fig. S5*B*, *Left* for quantitative characteristics of the sections cut ∼60 μm from the ID). The decrease in the amorphous halo indicates that hydrolysis has progressed at the IB. Retaining intensity in the amorphous halo suggests that the material near the OB of U-crests resists hydrolysis during the first 9 mo (see *SI Appendix*, Figs. S13–S22 for X-ray data and *SI Appendix*, Figs. S23–S25 for quantitative characteristics of all five 9 M sections).

The retention of the amorphous halo near the OB is also observed along line scans that are offset from the 9 M symmetry plane by ∼40 μm in the θ direction; the IB is susceptible to hydrolysis, while the amorphous halo at the OB is comparable to that of the as-deployed 0 M scaffold (relative to 0 M, the amorphous halo at IB has decreased more than 20% in 9 M; see Figs. 4*B* and 5*B* and *SI Appendix*, Fig. S5*B*, *Middle*). In contrast, microdiffraction line scans that are offset from the symmetry plane by ∼180 μm in the θ direction do not vary with position from IB to OB (Figs. 4*A* and 5*A*), consistent with the highly uniform morphology in portions of the scaffold that were undeformed during crimping and deployment. All of the patterns acquired ∼180 μm from the symmetry plane of 9 M show a weak amorphous halo similar to the IB near the symmetry plane (cf. Fig. 4 *A*–*C*, 15–20 μm; also see *SI Appendix*, Fig. S5*B*, *Right* and *SI Appendix*, Fig. S23, *Right*). The ability of the OB near the symmetry plane to resist degradation correlates with its unique microstructure (28), which only exists in regions subjected to elongational deformation during crimping.

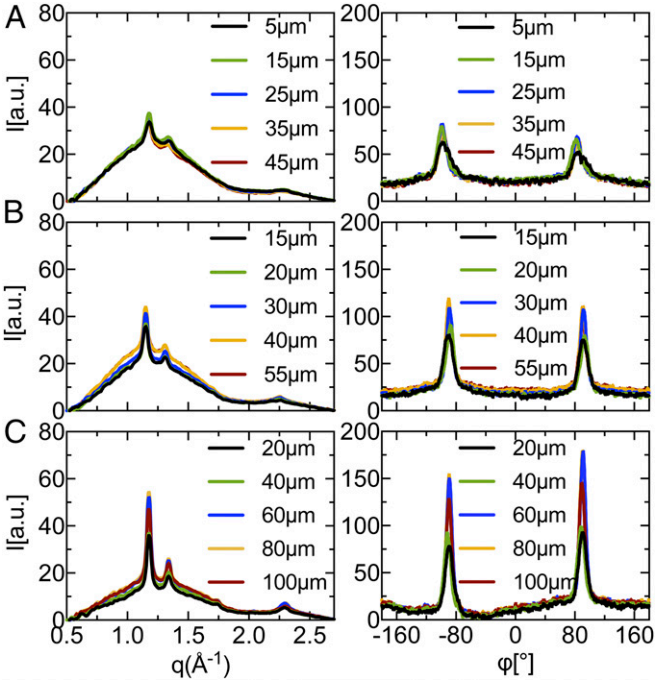

Fig. 3. Selected 1D microdiffraction profiles averaged (*Left*) azimuthally, I(*q*), and (*Right*) radially, I(φ) for WAXS patterns acquired on a section cut ∼60 μm from the ID of a (*A*) 0 M, (*B*) 9 M and (*C*) 18 M scaffold. The position at which each X-ray pattern was acquired is indicated in the legend (same positions as the 2D patterns in Fig. 2). Radial averaging was performed in the vicinity of the (110)/(200) reflection: $q \in [1.08–1.24\ Å^{-1}]$.

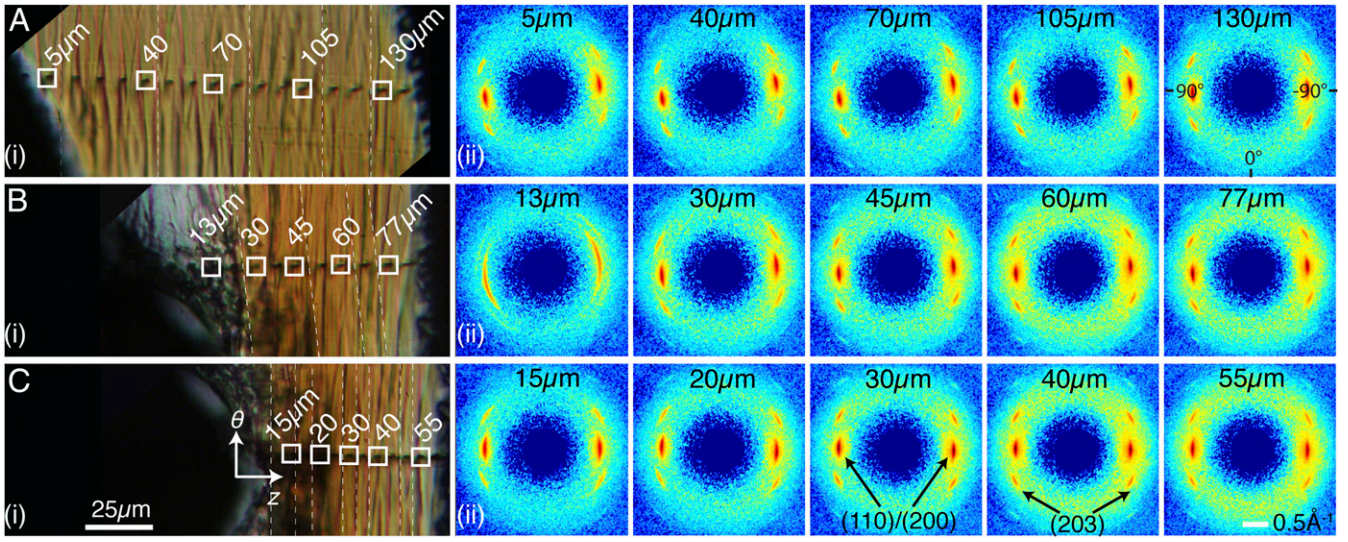

Fig. 4. Selected wide-angle X-ray microdiffraction patterns of the 9 M sample (section ~60 μm from the ID) acquired along lines that are (*A*) ~180 μm, (*B*) ~40 μm, and (*C*) ~0 μm from the symmetry plane. (*i*) Polarized light micrographs show the position of microdiffraction acquisitions (white squares labeled with their distance from the IB correspond to patterns in *ii*; white dashed lines indicate where images focused on specific X-ray marks were stitched together). (*ii*) Two-dimensional diffraction patterns use an identical logarithmic color scale [colors vary from 0 (deep blue) to 3 (deep red)] and *q*-scale (indicated at bottom right). Corresponding 1D patterns are given in Fig. 5 and quantitative characteristics of the amorphous and crystalline features of the 2D patterns are presented in *SI Appendix*, Fig. S5.

Discussion

There are four questions we consider in relation to our proposed resolution of the seemingly contradictory effects of hydrolysis on *Mn* and strength. Is the fraction of the scaffold that is resistant to hydrolysis small enough that the decrease in overall *Mn* could plausibly be dominated by the rest of the material? If the arms and links undergo faster hydrolysis than the U-crests, why do they remain intact at 9 mo? Is there evidence that loss of strength occurs first in the arms and links? Is there evidence that U-crests make particularly important contributions to scaffold radial strength? We address each of these in turn.

To estimate the fraction of the total material that resists hydrolysis in the scaffold, we use numerous optical and SEM images to calculate an upper bound for the volume of material near the OB that has a well-preserved amorphous halo at 9 M. We include material that is ~100 μm on each side of the symmetry plane of a deployed U-crest, which has an average IB-to-OB distance of ~80 μm and an average ID-to-OD thickness of ~140 μm. The resulting upper bound for the volume of material that resists degradation is $\sim 1.3 \times 10^{-3}$ mm^3 (mass ~1.7 μg per U-crest), which is <3% of the volume of scaffold per U-crest (*SI Appendix*, Fig. S26). The decrease in *Mn* as a function of hydrolysis time is evaluated by dissolving an entire scaffold for gel-permeation chromatography (GPC) measurements (*SI Appendix*, Fig. S1*A*); the GPC traces indicate that the presence of ~3% of chains that retain the initial distribution of molecular weights would be hidden under the GPC trace of the rest of the material (*SI Appendix*, Fig. S1*B*). Therefore, it is plausible that the apparent rate of hydrolysis averaged over the whole scaffold might not detect the local variations indicated by the microdiffraction results.

Our hypothesis might be perceived as creating another conundrum: If the arms and links are undergoing significant hydrolysis during the first 9 mo, how does the scaffold radial strength remain unchanged? The answer to this lies in the geometry of the cross-section of load-bearing elements and their orientation relative to the load. The links and arms have a substantially greater cross-section than the U-crests. Specifically, at the symmetry plane, the cross-section of the U-crest is ~70 μm × 140 μm, which is less than half that of the arms and links (135 μm × 150 μm). The links and arms are also oriented such that they either experience negligible stress during radial loading (links) or are subjected to a modest torque (arms). The combination of a large cross-section and little or no load being imposed results in negligible strain in these portions of the scaffold during radial loading. Consequently,

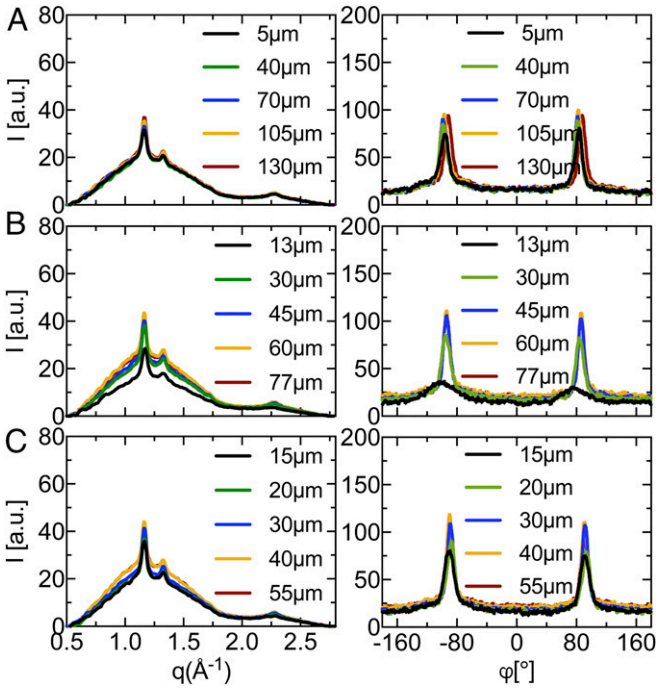

Fig. 5. Selected 1D microdiffraction profiles averaged (*Left*) azimuthally, I(*q*), and (*Right*) radially, I(*φ*), for WAXS patterns acquired on the 9 M sample (section ~60 μm from the ID) along lines located (*A*) ~180 μm, (*B*) ~40 μm, and (*C*) ~0 μm from the symmetry plane. Radial averaging was performed in the vicinity of the (110)/(200) reflection: $q \in [1.08–1.24$ Å$^{-1}]$. The legend indicates the position along the line (corresponding to the 2D patterns in Fig. 4).

the arms and links are unlikely to fail even if their strength decreases significantly during the first 9 mo.

If our hypothesis regarding the previously unexplained disconnect between the effects of hydrolysis on *Mn* and strength is correct, the drop in *Mn* in the arms and links might be accompanied by a decrease in strength. We checked for evidence that the links and arms lose strength earlier than the U-crests. Although the evidence we found is indirect and qualitative, it does accord with the expectation that strength decreases earlier where hydrolysis proceeds faster. First, in the sections cut from the scaffold after 18 mo of hydrolysis, many of the microtomed sections showed fissures extending in the θ direction entirely through a link (*SI Appendix*, Fig. S2 *A* and *B*, *Bottom*). Similarly, we saw several sections that had fissures extending in the θ direction entirely through an arm (*SI Appendix*, Fig. S2). In contrast, the U-crests were intact. Second, photographs of scaffolds after 20 mo and 22 mo of hydrolysis show that they fall apart in a way that leaves rings intact (*SI Appendix*, Fig. S27). In view of the small cross-section of the U-crests, it is surprising that the links break before the rings, which suggests that the links lose strength faster than the U-crests. Although this evidence is indirect, it is consistent with the hypothesis that hydrolysis in the majority of the scaffold proceeds faster than it does in the U-crests and that more rapid hydrolysis correlates with earlier loss of strength.

Finally, our resolution of the apparent disconnect between hydrolysis and scaffold strength depends on a small fraction of the scaffold as a whole—as little as 3%—having a disproportionate impact on the radial strength of the scaffold. It is known that U-crests are particularly important; upon overdeployment to failure, fractures predominantly occur in U-crests. By design, radial loading tends to impose tension and compression at the Y-, W-, and U-crests (defined in Fig. 1*A*). Among these, the U-crests have the smallest cross-section; consequently, U-crests are the sites where the material is subjected to the highest stress. Therefore, it is plausible that the small fraction of the total scaffold material (*ca.* 3%) that is located at the U-crests could play a particularly important role in scaffold strength.

The rest of the discussion is devoted to relating lessons learned from this study of the clinically approved scaffold to past and future scaffolds. After examining multiple scaffolds ($n = 3$ for scaffolds at each hydrolysis time), several U-crests per scaffold, many sections from each U-crest, and hundreds of diffraction patterns, we have observed that the materials and processing are consistent and reproducible. This is significant in light of substantial literature on PLLA that shows that hydrolysis kinetics and strength are sensitive to subtle changes in residual monomer content, *Mn*, and processing history (27). For example, inclusion of 7% monomer in compression-molded PLLA increased the rate of in vivo degradation by ∼66% during the first week (38). An increase in *Mn* has the opposite effect on the rate of degradation—an increase in chain length decreases the carboxyl group concentration, which in turn reduces the rate of hydrolysis (27). The PLLA morphology influences hydrolysis: Porosity accelerates degradation (34, 35), while PLLA crystallites are less susceptible to hydrolysis than amorphous material (26, 27, 33). Relatively subtle changes from the first- to second-generation Abbott BVS reduced the extent of hydrolysis in the first 18 M from the first-generation scaffold losing half its mass (7) to the second-generation BVS (the focus of this paper) losing only ∼10% of its initial mass over the same period (*SI Appendix*, Fig. S1*C*). Therefore, the degradation behavior of BVSs might be specific to the chemical composition of the PLLA and the particular processing conditions that were used.

The magnitude of the effects of material and processing is evident in a recent report on scaffolds that used a different PLLA grade, processing conditions, and laser-cut architecture for which the crimping process is detrimental to scaffold integrity (36). Among the differences in the processing conditions, the temperature during crimping may have contributed strongly to detrimental morphological changes during crimping: That study examined scaffolds crimped at room temperature (36), a temperature at which PLLA is brittle. Polarized Raman microscopy revealed that within 110 d the interior of the scaffold had lost crystallinity and orientation. Rapid degradation may result from residual monomer, lower stereoregularity, lower initial *Mn*, lower crystallinity, or some porosity. Some combination of these effects may be relevant to the scaffold that degrades rapidly. The study attributes rapid hydrolysis to crimping-induced gradients in morphology (36). In this paper, we reach a very different conclusion for scaffolds that are crimped in the vicinity of their glass transition temperature and undergo changes in morphology that increase strength and delay hydrolysis where it is needed most—in the U-crests (28).

Conclusions

The clinically approved BVS exhibits an intriguing trend with hydrolysis—it suffers a ∼40% decrease in the PLLA *Mn* after 9 mo of degradation, yet it has radial strength comparable to its initial state. This disconnect between *Mn* and radial strength has remained unresolved for nearly 10 y. Microdiffraction data acquired on a BVS hydrolyzed for 9 mo suggest that the lasting strength of the BVS has its origins in structural transformations created during crimping, particularly at U-crests. Crimping subjects the material in the vicinity of the symmetry plane of U-crests to tensile elongation at the OB, which increases the degree and orientation of crystallinity at the OB. This morphology created at the OB, which extends ∼100 μm across the symmetry plane of the U-crests, resists hydrolysis and provides strength where the cross-sectional area is the narrowest (at the diamond-shaped void, the IB-to-OB distance is ∼50 μm) and the stress is highest during radial loading. This region is so small (<3% of the total mass of the scaffold) that the *Mn* decrease measured for the scaffold as a whole could differ substantially from that in the U-crest (*SI Appendix*, Fig. S1*B*). We hypothesize that the measured *Mn* is dominated by the arms and links, which experience relatively low stress; therefore, the *Mn* in arms and links could drop significantly before it would alter the ability of the scaffold to withstand a radial load. It is the strength of the material at the point where stress is concentrated, here the U-crest, that governs the radial load the structure can support.

The future of bioresorbable scaffolds depends on further advances in materials. Clinically, the approved BVSs are associated with a higher incidence of definite or probable thrombosis than metal stents [∼1.3% for BVS vs. 0.6% for metal stents at the 12-mo follow-up; sample size: 3,253 patients received BVS and 2,315 received metal stents (13)]. Experts suspect the irregular blood flow over the 150-μm-thick device relative to the 80-μm-thick metal stents plays a role in thrombosis (13). The thin profile of metal stents also allows treatment of a wider range of lesions, including smaller and/or curved blood vessels. Thus, a stronger bioresorbable material is needed so that a thinner scaffold can support the blood vessel walls.

The present findings highlight the important role of processing in creating an unusually strong and hydrolysis-resistant morphology in PLLA. In the currently approved BVS, this morphology facilitates deployment (28) and maintains radial strength for months after implantation. The stark difference between another recent study (36) and the present study is reminiscent of the difference between the first- and second-generation BVS. Consequently, the ability of the OB of the clinically approved BVS to resist hydrolysis can be regarded as an existence proof that it is possible to tailor the PLLA microstructure to produce stronger PLLA and enable thinner scaffolds.

Materials and Methods

SEM of As-Deployed Scaffolds. Deployed scaffolds were mounted on SEM stubs using carbon tape and sputter-coated with gold to improve conductivity.

Micrographs were acquired on a Hitachi S-4800 field emission microscope at Abbott Vascular (Fig. 1*B*).

In Vitro Hydrolysis of Deployed Scaffolds. Scaffolds from the same batch of as-deployed BVSs were subjected to hydrolysis after deployment. The first group was removed from solution soon after deployment (0 M scaffolds) to halt hydrolysis and stored at −20 °C to prevent aging. The second and third groups were subjected to an additional 9 (9 M scaffolds) and 18 mo (18 M scaffolds) of hydrolysis in PBS at 37 °C before storage at −20 °C.

Microtoming Deployed Hydrolyzed Scaffolds. Microtomed sections of deployed, hydrolyzed scaffolds were provided by Abbott Vascular. Deployed scaffolds were first embedded in a methyl methacrylate-based medium (Technovit 7100, 120-min cure at 25 °C) and were then sectioned using a Powertome XL Ultra-Microtome. Consecutive 15-μm-thick sections were cut parallel to the θ–z plane of the scaffold from the OD surface to the ID surface (Fig. 1*C*). The microtome was maintained at −75 °C to minimize the impact of sectioning on the scaffold's microstructure.

Polarized Light Microscopy of the Microtomed Sections. Polarized light micrographs (magnification of 4×, 10×, and 32×) of deployed U-sections were acquired through crossed linear polarizers on a Zeiss Universal microscope equipped with a Cannon EOS DS30 camera for image acquisition. Composite 32× images were prepared by stitching individual images in Adobe Photoshop and Illustrator (boundaries indicated by dashed lines in Figs. 2 and 4 and *SI Appendix*, Figs. S8, S10, and S13–S17).

X-Ray Microdiffraction on Microtomed Sections of Deployed Scaffolds. Microdiffraction data were acquired at beamline 2-ID-D (200-nm spot size, $\lambda = 1.18$ Å) of the Advanced Photon Source at the Argonne National Labs. Images were acquired on a Mar165 CCD detector (2,048 × 2,048 pixels) at a sample to detector distance of 80.82 mm. Details regarding sample acquisition and background subtraction are provided in *SI Appendix*, Figs. S28–S33. A detailed description of the beamline optics can be found in the literature (39).

ACKNOWLEDGMENTS. We thank Dr. Zhonghou Cai (Advanced Photon Source, APS) for his assistance in collecting X-ray microdiffraction data and Troy Carter (Abbott Vascular) for sectioning the scaffolds. This research used resources of the APS, a US Department of Energy (DOE) Office of Science User Facility operated for the DOE Office of Science by Argonne National Laboratory under Contract DE-AC02-06CH11357. This work was supported by Abbott Vascular, the Jacobs Institute for Molecular Engineering for Medicine, and the National Heart, Lung, and Blood Institute of the National Institutes of Health under Award F31HL137308.

1. WHO (2010) *Global Atlas on Cardiovascular Disease Prevention and Control* (WHO, Geneva).
2. National Center for Health Statistics (2017) *Health, United States, 2016: With chartbook on long-term trends in health* (US Department of Health and Human Services, Washington, DC), DHHS Publ No 2017-1232, pp 18, 128–131.
3. Epstein AJ, Polsky D, Yang F, Yang L, Groeneveld PW (2011) Coronary revascularization trends in the United States, 2001-2008. *JAMA* 305:1769–1776.
4. Wiebe J, Nef HM, Hamm CW (2014) Current status of bioresorbable scaffolds in the treatment of coronary artery disease. *J Am Coll Cardiol* 64:2541–2551.
5. Ong DS, Jang I-K (2015) Causes, assessment, and treatment of stent thrombosis–Intravascular imaging insights. *Nat Rev Cardiol* 12:325–336.
6. Gomez-Lara J, et al. (2010) A comparison of the conformability of everolimus-eluting bioresorbable vascular scaffolds to metal platform coronary stents. *JACC Cardiovasc Interv* 3:1190–1198.
7. Oberhauser JP, Hossainy S, Rapoza RJ (2009) Design principles and performance of bioresorbable polymeric vascular scaffolds. *EuroIntervention* 5:F15–F22.
8. Kossuth MB, Perkins LEL, Rapoza RJ (2016) Design principles of bioresorbable polymeric scaffolds. *Interv Cardiol Clin* 5:349–355.
9. Ormiston JA, et al. (2012) First serial assessment at 6 months and 2 years of the second generation of absorb everolimus-eluting bioresorbable vascular scaffold: A multimodality study. *Circ Cardiovasc Interv* 5:620–632.
10. Serruys PW, et al. (2016) A polylactide bioresorbable scaffold eluting everolimus for treatment of coronary stenosis: 5-year follow-up. *J Am Coll Cardiol* 67:766–776.
11. Iqbal J, et al. (2014) Bioresorbable scaffolds: Rationale, current status, challenges, and future. *Eur Heart J* 35:765–776.
12. Serruys PW, et al. (2015) A bioresorbable everolimus-eluting scaffold versus a metallic everolimus-eluting stent for ischaemic heart disease caused by de-novo native coronary artery lesions (ABSORB II): An interim 1-year analysis of clinical and procedural secondary outcomes from a randomised controlled trial. *Lancet* 385:43–54.
13. Kang J, et al. (2017) Bioresorbable vascular scaffolds–Are we facing a time of crisis or one of breakthrough? *Circ J* 81:1065–1074.
14. Rizik DG, Shah MG, Burke RF (2016) First US experience following FDA approval of the ABBOTT vascular bioresorbable vascular scaffold for the treatment of coronary artery disease. *Catheter Cardiovasc Interv* 88:899–901.
15. Langer R, Tirrell DA (2004) Designing materials for biology and medicine. *Nature* 428:487–492.
16. Tibbitt MW, Rodell CB, Burdick JA, Anseth KS (2015) Progress in material design for biomedical applications. *Proc Natl Acad Sci USA* 112:14444–14451.
17. Kang S-K, et al. (2016) Bioresorbable silicon electronic sensors for the brain. *Nature* 530:71–76.
18. Rolland JP, et al. (2005) Direct fabrication and harvesting of monodisperse, shape-specific nanobiomaterials. *J Am Chem Soc* 127:10096–10100.
19. Renouf-Glauser AC, Rose J, Farrar DF, Cameron RE (2005) The effect of crystallinity on the deformation mechanism and bulk mechanical properties of PLLA. *Biomaterials* 26:5771–5782.
20. Nakafuku C, Takehisa SY (2004) Glass transition and mechanical properties of PLLA and PDLLA-PGA copolymer blends. *J Appl Polym Sci* 93:2164–2173.
21. Hu Y, Rogunova M, Topolkaraev V, Hiltner A, Baer E (2003) Aging of poly(lactide)/poly(ethylene glycol) blends. Part 1. Poly(lactide) with low stereoregularity. *Polymer* 44:5701–5710.
22. Broz ME, VanderHart DL, Washburn NR (2003) Structure and mechanical properties of poly(D,L-lactic acid)/poly(ε -caprolactone) blends. *Biomaterials* 24:4181–4190.
23. Rathi S, et al. (2011) Toughening semicrystalline poly(lactic acid) by morphology alteration. *Polymer* 52:4184–4188.
24. Grijpma DW, Pennings AJ (1994) (Co) polymers of L-lactide, 1. Synthesis, thermal properties and hydrolytic degradation. *Macromol Chem Phys* 195:1633–1647.
25. Huang MH, Li S, Vert M (2004) Synthesis and degradation of PLA-PCL-PLA triblock copolymer prepared by successive polymerization of ε-caprolactone and DL-lactide. *Polymer* 45:8675–8681.
26. Li S, Garreau H, Vert M (1990) Structure-property relationships in the case of the degradation of massive poly (α-hydroxy acids) in aqueous media, Part 3: Influence of the morphology of poly (L-lactic acid). *J Mater Sci Mater Med* 1:198–206.
27. Li S (1999) Hydrolytic degradation characteristics of aliphatic polyesters derived from lactic and glycolic acids. *J Biomed Mater Res* 48:342–353.
28. Ailianou A, Ramachandran K, Kossuth MB, Oberhauser JP, Kornfield JA (2016) Multiplicity of morphologies in poly (l-lactide) bioresorbable vascular scaffolds. *Proc Natl Acad Sci USA* 113:11670–11675.
29. Ramachandran K, et al. (2018) Tube expansion deformation enables in situ synchrotron x-ray scattering measurements during extensional flow-induced crystallization of poly l-lactide near the glass transition. *Polymers* 10:288.
30. Leenslag JW, Pennings AJ, Bos RRM, Rozema FR, Boering G (1987) Resorbable materials of poly(L-lactide). VII. In vivo and in vitro degradation. *Biomaterials* 8:311–314.
31. Rapoza R, Veldhof S, Oberhauser J, Hossainy SFA (2015) Assessment of a drug eluting bioresorbable vascular scaffold. US Patent Application 14/121,435.
32. Tsuji H, Ogiwara M, Saha SK, Sakaki T (2006) Enzymatic, alkaline, and autocatalytic degradation of poly(L-lactic acid): Effects of biaxial orientation. *Biomacromolecules* 7:380–387.
33. Tsuji H, Mizuno A, Ikada Y (1999) Properties and morphology of poly (L-lactide). III. Effects of initial crystallinity on long-term in vitro hydrolysis of high molecular weight poly(L-lactide) film in phosphate-buffered solution. *J Appl Polym Sci* 77:1452–1464.
34. Pistner H, et al. (1994) Poly(L-lactide): A long-term degradation study in vivo. Part II: Physico-mechanical behaviour of implants. *Biomaterials* 15:439–450.
35. Pistner H, Bendix DR, Mühling J, Reuther JF (1993) Poly(L-lactide): A long-term degradation study in vivo. Part III. Analytical characterization. *Biomaterials* 14:291–298.
36. Wang P-J, Ferralis N, Conway C, Grossman JC, Edelman ER (2018) Strain-induced accelerated asymmetric spatial degradation of polymeric vascular scaffolds. *Proc Natl Acad Sci USA* 115:2640–2645.
37. Pantani R, De Santis F, Auriemma F, De Rosa C, Di Girolamo R (2016) Effects of water sorption on poly (lactic acid). *Polymer* 99:130–139.
38. Nakamura T, et al. (1989) Bioabsorption of polylactides with different molecular properties. *J Biomed Mater Res* 23:1115–1130.
39. Cai Z, et al. (2000) A hard x-ray scanning microprobe for fluorescence imaging and microdiffraction at the Advanced Photon Source. *AIP Conference Proceedings* (AIP Publishing, Melville, NY), Vol 507, pp 472–477.